REGULAR PAPER



Studying Crack Generation Mechanism in Single-Crystal Sapphire During Ultra-precision Machining by MD Simulation-Based Slip/Fracture Activation Model

Suk Bum Kwon¹ · Aditya Nagaraj¹ · Dalei Xi² · Yiyang Du² · Dae Nyoung Kim¹ · Woo Kyun Kim² · Sangkee Min¹

Received: 27 July 2022 / Revised: 29 December 2022 / Accepted: 7 February 2023 / Published online: 9 March 2023 © The Author(s), under exclusive licence to Korean Society for Precision Engineering 2023

Abstract

Single-crystal sapphire is used in various fields of industry due to its superior mechanical, optical, and chemical properties, but fabricating sapphire is challenging because of its high hardness and brittleness. Ultra-precision machining (UPM) has been studied as one of the solutions to overcome these issues as it facilitates cutting of brittle ceramics in a ductile manner. However, the material removal mechanisms during UPM of single-crystal sapphire is not yet fully understood. This paper studied the crack initiation mechanism in single-crystal sapphire during UPM with relation to the crystallographic properties of sapphire depending on the cutting direction. By projecting a given stress distribution from molecular dynamics simulation on to different slip and fracture planes, the likelihood of plastic deformation and cleavage fracture was calculated, and respective crack initiation mechanisms were identified. The proposed MD simulation model and analysis were verified through ultra-precision orthogonal plunge cut experiments along the same crystallographic directions as the simulations.

 $\textbf{Keywords} \ \ Ultra-precision \ machining \cdot Single-crystal \ sapphire \cdot Ductile-to-brittle \ transition \cdot Molecular \ dynamics \cdot Slip/fracture \ activation \ model$

1 Introduction

Ceramics such as sapphire (α -Al₂O₃) are widely used in applications under harsh environments such as space probes, corrosive chemical environments, and ballistic windows due to their superior mechanical, thermal, and optical properties [1, 2]. Sapphire belongs to the ditrigonal scalenohedral crystal class and space group 167 having $R\overline{3}c$ symmetry [3]. The crystal structure comprising of a hexagonal unit cell, along with the four functional crystallographic planes (A, C, M, and R) is represented in Fig. 1 [2].

Pronounced hardness, brittleness, and crystal anisotropy have been some of the major challenges while processing ceramics. In addition to this, machining of ceramics has been

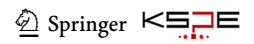
This paper was presented at PRESM2022.

- Sangkee Min sangkee.min@wisc.edu
- Department of Mechanical Engineering, University of Wisconsin-Madison, Madison, WI 53706, USA
- Department of Mechanical and Materials Engineering, University of Cincinnati, Cincinnati, OH 45221, USA

known to create residual stresses and subsurface damage that can cause failure through crack propagation at premature stress levels [4]. Overcoming these challenges during ultraprecision machining has been difficult due to various factors and uncertainties that influence the machining process at the micro-nano scales and difficulties associated with characterization of ultra-precision machined surfaces and associated subsurface damage. As a result, our understanding of material deformation during ultra-precision machining is far from complete.

To better understand the material removal behavior of single-crystal ceramics during ultra-precision machining, research based on experiments and analytical models have been conducted. Mizumoto et al. [5] performed ultra-precision orthogonal plunge cutting along various directions on the C-plane of sapphire, and the slip/fracture activation model was used to explain how plastic deformation and cleavage fracture occur on specific crystallographic planes and how different cutting orientations affect the material removal behavior.

The slip/fracture activation model calculates and ranks the likelihood of slip/twinning or crack initiation on the available slip/fracture systems using the Schmid factor



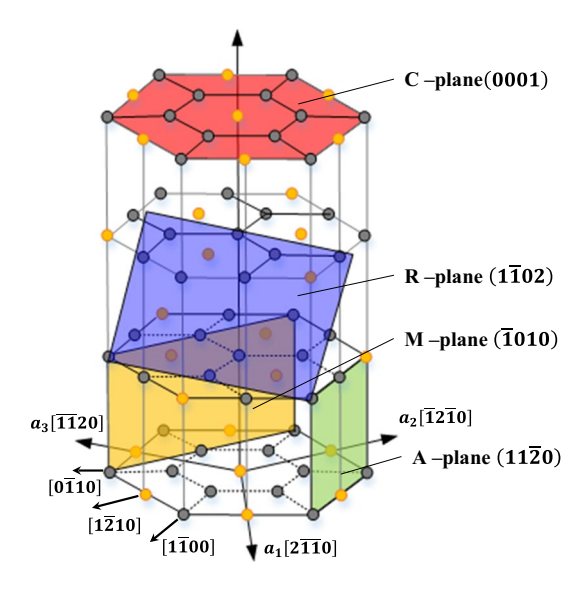


Fig. 1 Crystallographic structure of single-crystal sapphire [2]

and normalizing over the critical resolved shear stress and critical stress intensity factor respectively. Kwon et al. [6] modified the slip/fracture activation model for a more accurate calculation of plastic deformation and cleavage fracture parameters by accounting for the changes in the thrust force with the depth of cut. Using this approach, the authors studied the effect of crystalline structure and cutting force on material removal behavior on the R-plane of sapphire and analyzed the anisotropic distribution of critical depth of cut (CDC)—depth of cut at which ductile-brittle transition occurs, and diversity of crack morphology [7]. Apart from this, the slip/fracture activation model has been used to describe material removal behavior in terms of CDC and crack morphology for other single-crystal ceramics such as YSZ (Yttria-Stabilized Zirconia) and CaF₂ during UPM as well [8, 9].

These studies have shown that the slip and fracture activations on various crystal planes dominantly affect the material removal behavior during ultra-precision machining of single-crystal ceramics. However, the limitation of the slip/fracture activation model is that the model only uses the force values as an input and cannot consider the contributions from a 3-dimensional stress field which provides a more realistic representation of machining.

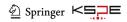
An alternate route to further our understanding and investigate the basic mechanisms of material deformation at the nanoscale is through computer simulation techniques such as molecular dynamics (MD) and smooth particle hydrodynamics (SPH) simulations. Surface and subsurface damage during deformation of different single crystalline ceramics have been investigated by various researchers using different approaches. In general, at the atomic scale, deviation from the crystal structure of the

bulk material due to an applied load can be regarded as damage as this would change the properties of the material, thus affecting the functionality of the ceramic material. In micro- and meso-scale simulations, this definition is extended to include dislocations, micro-cracks, phase changes, and other micro-structures that alter the properties of the ceramic.

MD simulations of scratch tests on silicon using a conical indenter indicated that as the half-angle of the cone was increased, the degree of phase transformation observed also increased due to the higher hydrostatic stress state generated by the large negative rake angle of the indenter. Additionally, the researchers also reported an increase in the subsurface damage depth as the half-angle of the cone was increased [10]. Similar studies comparing traditional machining to laser-assisted machining showed that laser heating reduced the cutting and tangential forces and at the same time, predicted lesser subsurface damage through localized deformation around the region heated by the laser [11]. The analyses in both studies were carried out by calculating the coordination numbers of the deformed atoms and comparing them with the coordination numbers of known crystal polytypes of silicon.

Li et al. investigated the effect of various process parameters and crystal orientations on subsurface damage during scratch tests in single-crystalline copper through MD simulations. The analysis was carried out through different methods such as dislocation visualization, common neighbor analysis, and surface height mapping. It was reported that increasing scratch speed, decreasing the tool diameter, and smaller depths of cut reduced the subsurface damage [12]. Liu et al. performed a similar analysis on SiC and reported that increasing the depth of cut had a greater effect on the subsurface damage depth than increasing the cutting speed [13]. In a parallel study, the authors increased the size of the simulation using smooth particle hydrodynamics and were able to observe ductile-brittle transition and the effect of process parameters on deformation remained similar [14]. Dai et al. investigated the effect of tool geometry on subsurface damage in single crystalline silicon through MD simulations and reported that positive rake angle and small edge radius reduce the subsurface damage [15]. In a study on subsurface damage in Ni/Cu multilayers, Fang et al. reported a higher amount of subsurface damage in the multilayered specimen compared to a standalone Ni thin film. However, the dislocations generated in the top layer of the multilayer specimen were largely absorbed by the interface thus limiting the depth of subsurface damage [16].

MD simulations have also been conducted to investigate the deformation and failure mechanism of sapphire. For example, Chang et al. used MD simulations to study the core structure of pyramidal dislocations in sapphire [17].



Wunderlich et al. studied the crack propagation and fracture toughness in sapphire using MD method [18].

Nucleation of rhombohedral twinning in sapphire was observed and investigated by Kuksin et al. with the MD shockwave model [19]. Nishimura et al. performed MD nanoindentation simulations on multiple crystallographic planes of sapphire to examine the effect of surface orientation on plastic deformation processes [20]. Lin et al. performed both MD nanoindentation and scratching test on the C-planes of sapphire [21]. The surface morphology of the C-planes and deformation activation during the machining process were analyzed and compared with experimental results. MD simulations of nano-scale cutting, indentation and scratching tests on sapphire conducted by Kim et al. [22, 23], which revealed the underlying deformation mechanism and anisotropy of sapphire during ultra-precision machining. From the survey of previous literature, a gap in the understanding of crack initiation-based crystallographic orientation and stress field has been identified.

In this paper, the crack initiation mechanism in single-crystal sapphire during ultra-precision machining was studied in relation to the slip/fracture activation model based on the stress field calculated from molecular dynamics simulations. The results from MD simulations were compared with and validated using experimental results.

2 Materials and Methods

2.1 Molecular Dynamics (MD) Simulations

Molecular Dynamics simulations have been widely used in material analysis due to its advantages on manipulability and ease in analysis. However, due to its computational limitations, the size and strain rate differences between simulations and experimental samples cannot be escaped. Although it is difficult to compare results quantitatively, qualitative similarities are observed across simulation and experimental results.

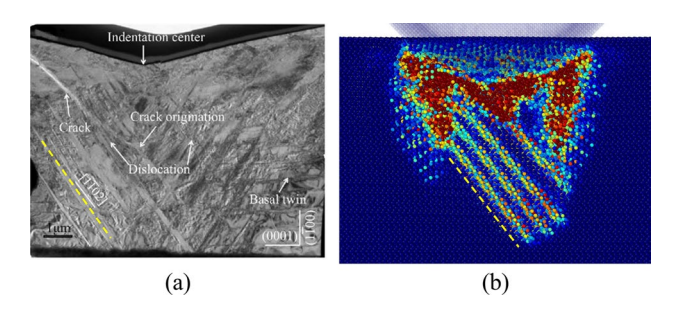


Fig. 2 Comparison between the $\bf a$ experimental and $\bf b$ simulation results during C-plane indentation. In both figures the dashed lines indicate the rhombohedral twin planes

Figure 2 compares the cross sections after the indentation test on C-plane of sapphire from the experiment [24] and MD simulation [22]. It is observed that the MD simulation shows a similar resultant rhombohedral twinning as shown in the TEM image, and it showcases MD simulations' capability in reproducing similar deformation mechanisms as larger scale experiments.

The simulation model consisted of a rectangular sapphire substrate with approximate dimensions of $1500 \text{ Å} \times 30 \text{ Å} \times 1000 \text{ Å}$ in the x, y, and z directions, respectively, comprising about 4,500,000 atoms as shown in Fig. 3. Periodic boundary condition (PBC) was applied in the y direction. The outermost layers of atoms on the bottom and one side were fixed to prevent any rigid body translations and a Langevin thermostat region was assigned just adjacent to the fixed layer to absorb any excess heat generated from the deformation. The region above the thermostat region, assigned as the Newtonian region, was the region where the deformation occurs. The tool used in the cutting simulation had an edge radius of 60 Å and a rake angle of -10°, modeled as a rigid body having a diamond cubic structure consisting of about 68,500 atoms. MD simulations of orthogonal cutting on the C-plane of sapphire were conducted using LAMMPS (Large-scale Atomistic/Molecular Massively Parallel Simulator) [25]. The cutting simulations were performed in the $|\overline{11}20|$ and $|\overline{1}100|$ directions at a cutting depth

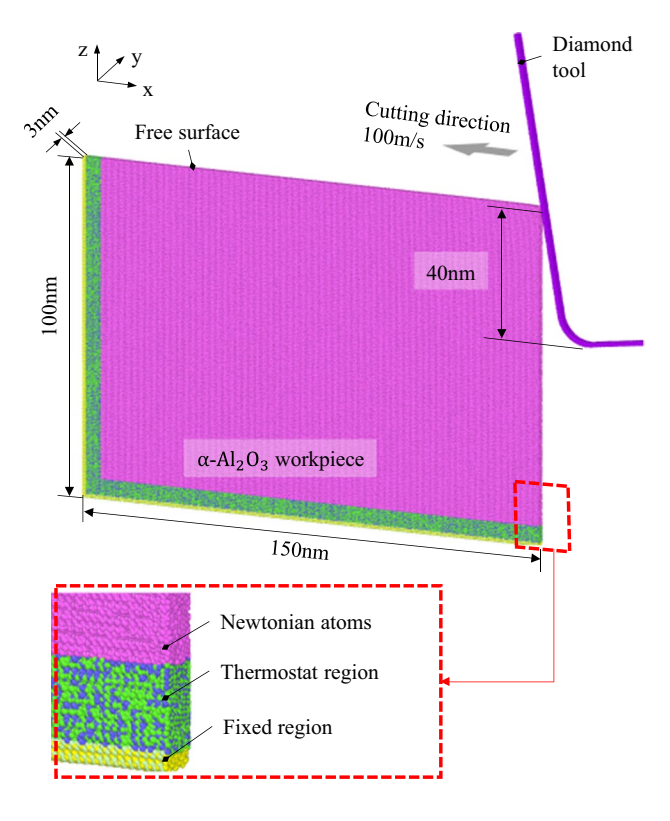
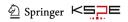


Fig. 3 Setup of molecular dynamics simulation of UPM on C-plane of sapphire



of 400 Å and cutting speed of 100 m/s for a cutting length of over 1000 Å, Fig. 4a. Figure 4b, c show the side view of the crystallographic structure along $\left[\overline{11}20\right]$ and $\left[\overline{1}100\right]$ directions, respectively.

Multiple interatomic potentials have been used to study sapphire such as charge optimized many body (COMB) potential [26], modified embedded atom model (MEAM) potential [27], Coulomb-Buckingham potential [28] and Vashishta potential [29] among many others. In this study, Vashishta potential consisting of two- and three-body terms was employed to describe the interactions between atoms in sapphire due to its capability to properly describe the properties of sapphire such as the elastic constants, bulk modulus, cohesive energy and melting temperature. The interactions between the tool and substrate atoms (i.e. C–Al and C–O) were modeled through the Lennard–Jones potential [16, 30]

2.2 Normal and Shear Stresses Acting on a Crystal Plane

From the MD simulations, stress tensor at different points in the material can be obtained by computing the per-atom stress on each atom. Given the Cauchy stress distributions at different points in the material and information on directions of plane normal, slip and cleavage, the normal and

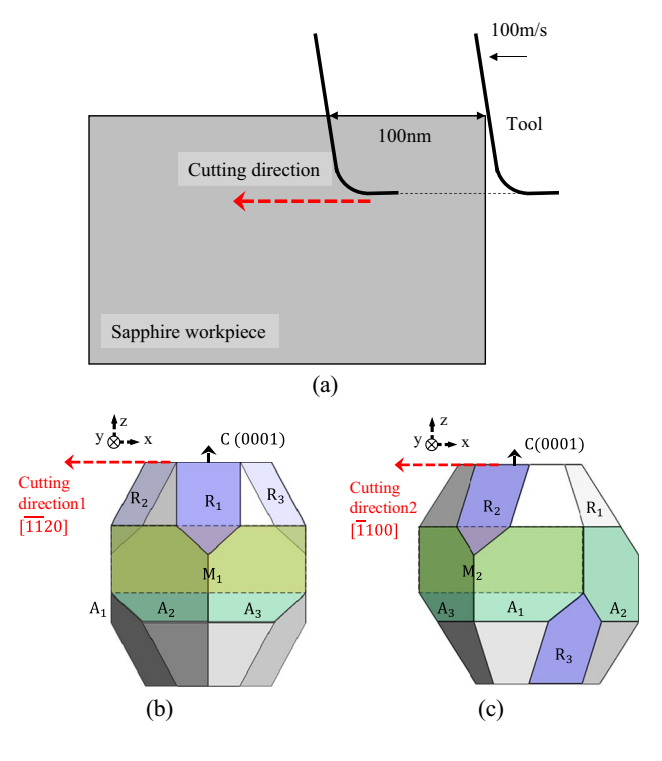


Fig. 4 a Schematic view of cutting simulation and crystallographic structure orientation along different cutting directions $\mathbf{b} \begin{bmatrix} \overline{11}20 \end{bmatrix}$, and $\mathbf{c} \begin{bmatrix} \overline{11}00 \end{bmatrix}$ from the side view

shear stresses acting on a crystal plane can be calculated using Eq. 1.

$$T_i = \sigma_{cauchy} \cdot n_i \tag{1}$$

where T_i is the traction vector on the *i*th crystal plane, σ_{cauchy} is the Cauchy stress tensor at a given point, and n_i is the normal unit vector of the *i*th crystal plane. The normal stress and shear stress along the slip/fracture direction on the *i*th crystal plane, σ_i and τ_i , can be calculated using Eqs. 2 and 3.

$$\sigma_i = n_i \cdot T_i \tag{2}$$

$$\tau_i = \left(s_i \cdot d_i\right) \left(\sqrt{\left|T_i\right|^2 - \sigma_i^2}\right) \tag{3}$$

where σ_i is the normal stress on the *i*th crystal plane, Fig. 5a, τ_i is the shear stress along the slip/twinning direction on the *i*th crystal plane, s_i is the unit direction vector along the slip/twining on the *i*th crystal plane, and d_i is the unit direction vector along the shear stress on the *i*th crystal plane obtained by projection of T_i on to the *i*th crystal plane as shown in Fig. 5b.

2.3 Calculating Likelihood of Plastic Deformation and Cleavage Fracture Based on Slip/fracture Activation Model

Another way to describe the machining characteristics in terms of crystallographic orientation is by calculating deformation activation parameters based on the slip/fracture activation model. The benefit of using this parameter are the normalized output values which allows for easier comparison between

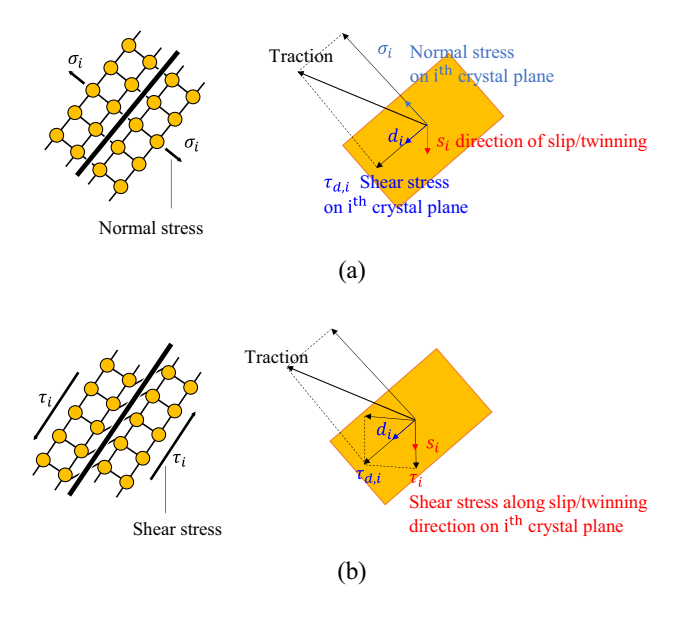
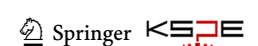


Fig. 5 Calculation of **a** normal stress and **b** shear stress along the slip/twinning direction on the i^{th} crystal plane



likely deformation mechanisms. The slip/fracture activation model calculates the likelihood of plastic deformation and cleavage fracture as shown in Fig. 6a, b using Eq. 4 and Eq. 5 [5, 6].

$$P_{i} = \left\{ \cos(\theta_{i})\cos(\lambda_{i}) \right\} \min_{i}(\tau_{CRSS})/\tau_{CRSS,i}$$
(4)

$$F_j = \left\{ \cos^2(\theta_j) \right\} \min_j (K_{IC}) / K_{IC,j}$$
 (5)

where P_i is the plastic deformation parameter, indicating the likelihood of plastic deformation on the *i*th crystal plane, and

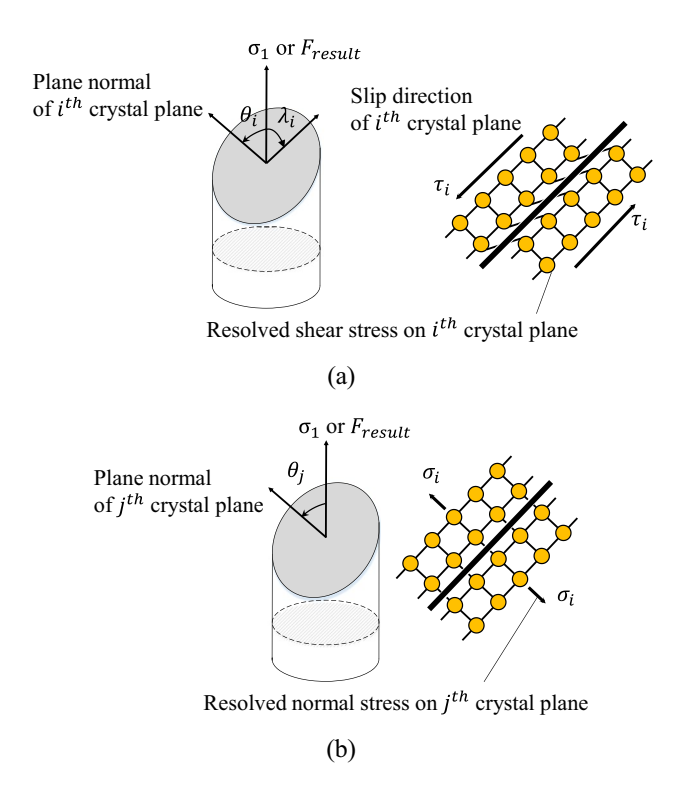


Fig. 6 Angular relationships used in the a slip and the b fracture activation

Table 1 Slip/twinning systems of single-crystal sapphire [31]

Slip/twinning system	Miller-Bravais indices	Critical Resolved Shear Stress [MPa]
Basal twinning (C-plane)	(0001) < 1010>	2.2255
Basal slip (C-plane)	(0001) < 1120>	2.2255
Pyramidal slip	{0111} <1011>	4.4817
Prismatic slip (A-plane)	{1120} < 1100>	1.6487
Rhombohedral twin- ning (R-plane)	{1102} <1101>	0.4066

Table 2 Fracture systems of single-crystal sapphire [32]

Fracture system	Miller-Bravais indices	Critical stress intensity factor (MPa m ^{-1/2})
Basal fracture (C-plane)	(0001)	4.54
Prismatic fracture (M-plane)	$\{10\overline{1}0\}$	3.14
Rhombohedral fracture (R-plane)	{1102}	2.38
Prismatic fracture (A-plane)	{1120}	2.43

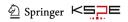
 F_j is the cleavage fracture parameter, indicating the likelihood of cleavage fracture on the jth crystal plane. $\min_i(\tau_{CRSS})$ is the minimum value of critical resolved shear stress, and $\tau_{CRSS,i}$ is the critical resolved shear stress of the ith crystal plane. $\min_j(K_{IC})$ is the minimum value of mode I critical stress intensity factor, and $K_{IC,j}$ is the mode I critical stress intensity factor of the jth crystal plane. The values of critical resolved shear stress and critical stress intensity factor are indicated in Table 1 and Table 2 respectively.

The terms $cos(\theta_i)cos(\lambda_i)$ and $cos^2(\theta_j)$ can be physically interpreted as the ratio between uniaxial applied normal stress to resolved normal stress on the *i*th crystal plane and uniaxial applied normal stress to resolved shear stress on the *j*th crystal plane, respectively. The term $cos(\theta_i)$ is the cosine between resultant force F_{result} and the plane normal vector of the *i*th crystal plane, and the term $cos(\lambda_i)$ is the cosine between resultant force and slip/twinning direction of the *i*th crystal plane, Fig. 6a. The term $cos(\theta_j)$ is the cosine between the resultant force and the plane normal vector of the *j*th crystal plane as shown in Fig. 6b. The angle made by the resultant force with the surface, θ_{result} , is calculated using Eq. 6.

$$\theta_{\text{result}} = \operatorname{atan}\left(\frac{F_{cut}}{F_{thrust}}\right) \tag{6}$$

where F_{cut} and F_{thrust} are the cutting force and the thrust force measured by a piezoelectric dynamometer during the machining process, respectively.

Although the analysis based on resultant force provides useful insight into material deformation, calculations based on the stress distribution can provide more details as the experimental measurements are orthogonal. As the slip/fracture model originally uses the resultant force vector as an input, modifications are necessary when the stress tensor is instead used as an input. When the Cauchy stress is used, $\cos(\theta_i)$ becomes the cosine between the maximum principal stress σ_1 and plane normal unit vector of the *i*th crystal plane, and $\cos(\lambda_i)$ becomes the cosine between σ_1 and slip/twinning direction of the *i*th crystal plane, Fig. 6a. And $\cos(\theta_j)$ becomes the cosine between σ_1 and plane normal of the *j*th crystal plane, Fig. 6b. The direction of the maximum



principal stress n_1 can be obtained by solving the following eigen value equation.

$$(\sigma_{cauchy} - \lambda_1 \mathbf{I}) \mathbf{n}_1 = 0 \tag{7}$$

where σ_{cauchy} is the Cauchy stress tensor at a given point obtained from MD simulations, λ_1 is the eigen value equal to maximum principal stress, and n_1 is the eigenvector in the direction of the plane normal where maximum principal stress is applied.

In this paper, the material removal behavior in MD simulation was analyzed based on two different approaches: (1) normal stress and shear stress method introduced in Sect. 2.2. and (2) plastic deformation and cleavage fracture parameter method introduced in Sect. 2.3.

3 Experiment

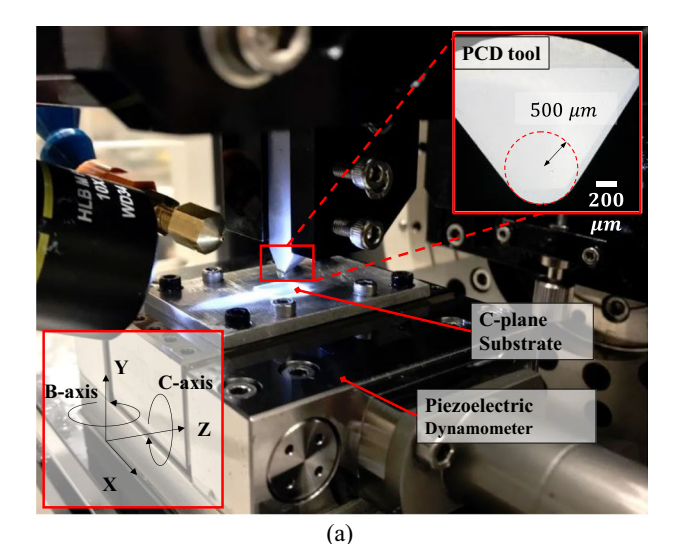
For the experiment, ultra-precision orthogonal plunge cutting on C-plane of sapphire was conducted. A 5-axis ultra-precision CNC machine with 1 nm command resolution in the 3 linear axes and 1 micro-degree command resolution in the 2 rotary axes was used with a binderless nano-polycrystalline diamond tool with 0.5 mm nose radius. The substrate was mounted on a piezoelectric dynamometer to measure the cutting and thrust forces. Figure 7a shows the experimental setup. Cutting was performed at 5 mm/min cutting speed and 1/500 tool path slope in the $\boxed{1120}$ and $\boxed{1100}$ orientations (similar to the MD simulations) as shown in Fig. 7b. For repeatability, the cutting in each direction was repeated 3 times. Crack morphologies on the machined surfaces were observed using an optical microscope and scanning electron microscope (SEM, Zeiss 1530).

4 Results and Discussion

4.1 Calculating Normal Stress and Shear Stress on Crystal Plane

The MD simulations results were analyzed for two different cutting directions, $[\overline{11}20]$ and $[\overline{1}100]$ up to 250 ps, which is 80 ps post first crack initiation in the $[\overline{1}100]$ cutting direction. By using common neighbor analysis and shear strain color-coding functions in OVITO [33], the local crystal structure and shear strains were plotted.

Figure 8c-f show the evolution of crystallographic structure and shear strain as cutting progresses in the $\left[\overline{1120}\right]$ cutting direction. A dominant shear strain parallel to the cutting direction was observed as the cutting



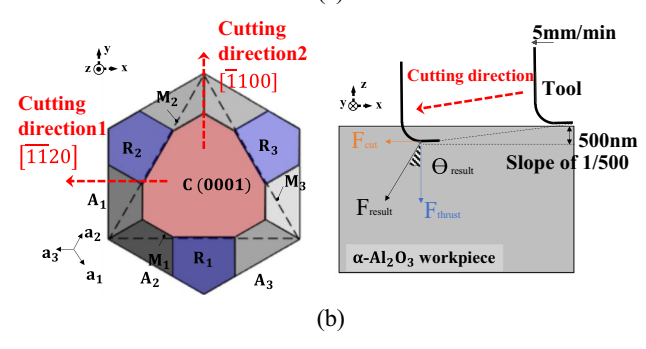
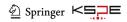


Fig. 7 a Experimental setup and \mathbf{b} schematic view of orthogonal plunge cutting

progressed further into the workpiece, indicated by the yellow arrows. Referring to the crystallographic structure shown in Fig. 8a, b, this direction matched with the direction of basal slip (C_{sl}) and twinning systems (C_{tw}) .

For further analysis, normal and shear stresses acting on the various crystal planes were calculated. As this study focuses on crack initiation and propagation, this analysis was focused on a point (point A)—which exhibited large value of tensile normal stress and a likely location for crack initiation. The analysis region was a square with a size of 300 nm by 300 nm around point A, Fig. 9a. The highest magnitudes of normal stresses on different crystallographic planes were then plotted with respect to time for the atomic positions within the box. Even though the location of point A changed continuously in terms of time, tensile normal stress on C-plane had a higher magnitude compared to other planes, Fig. 9b.

The highest tensile normal stress occurred on the C-plane at point A, at 170 ps cutting time (red arrows in Fig. 9b). Figure 9c, d show the normal stress and shear stress on the C-plane at point A. A crack initiation was not observed in this direction.



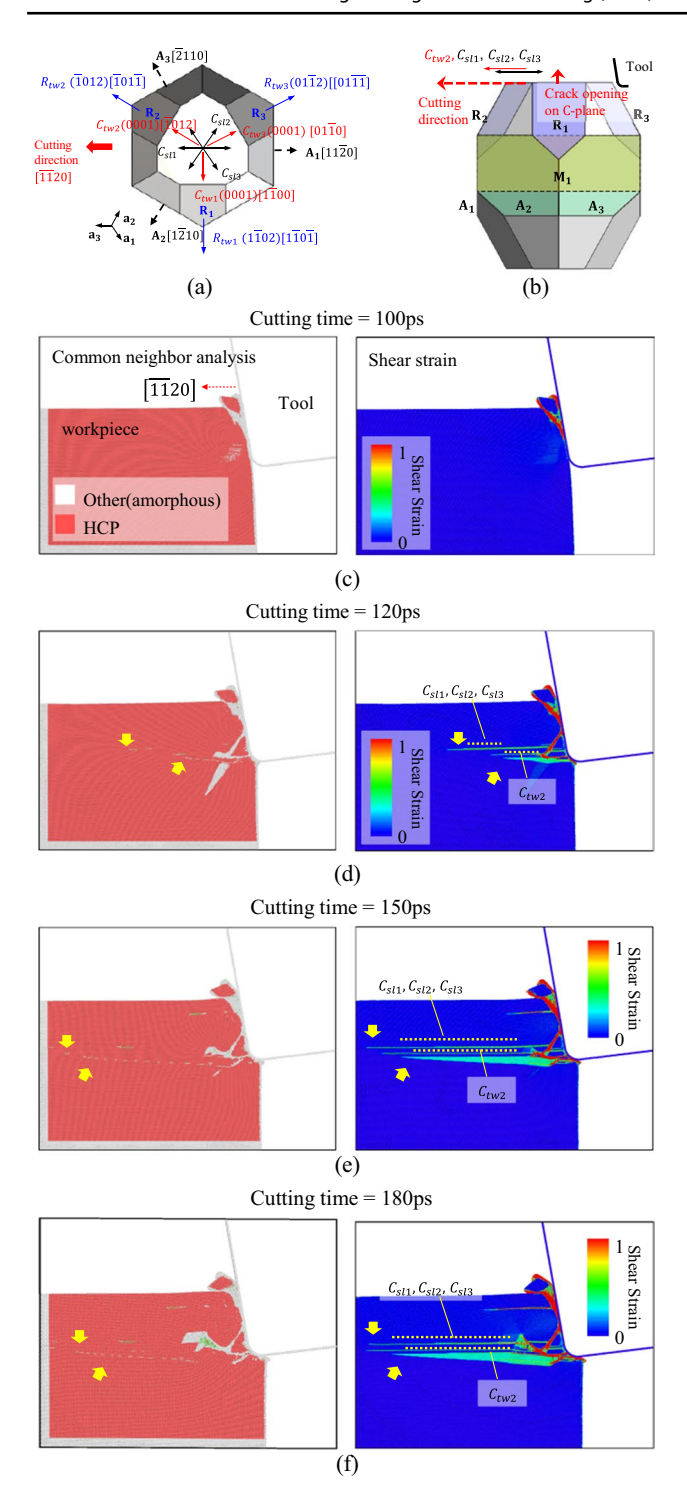


Fig. 8 The schematic view of cutting orientation in **a** top view and **b** side view. Common neighbor analysis and shear strain in terms of cutting time at **c** 100 ps, **d** 120 ps, **e** 150 ps, and **f** 180 ps

In Fig. 9c, the normal stress on the C- plane dramatically decreased from 17 to 0 GPa without crack initiation. This happens as the shear strain is generated parallel to the cutting orientation and stress is accumulated in front of the tool.

Most of the stressed region is removed by chip forming as the tool keeps moving forward into the workpiece. Also, a high amount of shear stress on C_{sl1} , C_{sl2} , C_{sl3} and C_{tw2} slip/twinning systems were observed. The amount of shear stress along these directions showed a periodic increase and reduction, Fig. 9d. This is likely due to activation of slips/twinning on the C-plane only when the stresses reach a critical value until which point an increase in stress is observed.

Figure 10c-f show the results of common neighbor analysis and shear strain along the $|\overline{1}100|$ cutting orientation. Although all the process parameters were similar to the 1120 cutting direction, the material removal behavior was very different because of the effect of crystallographic orientation. A crack appeared at a cutting time of 180 ps and its opening direction was parallel to C-plane normal (red arrow). From the beginning of machining to the moment when the crack was initiated, high shear strain, diagonal to the cutting direction was observed, indicated by yellow arrows in Fig. 10c-f. The location where the crack was initiated was set as point B. In the area surrounding point B, amorphous structure was observed just prior to crack initiation but the crystal structure reverted back to the hexagonal closed pack (HCP) structure soon after, shown in Fig. 10d, e. The reason for this structural transformation was due to large stress accumulation in front of the tool which changed the position of the atoms from the equilibrium values but as the stresses were relieved by crack initiation, the atoms return to the equilibrium position assuming the HCP structure once again. The direction of basal fracture and rhombohedral R_{2tw} and R_{3tw} twinning systems matched with the direction of crack opening and shear strains, Fig. 10a, b, respectively.

Further, normal and shear stresses on different crystal planes were calculated around point B, Fig. 11a-d. This analysis was focused on a point (point B) - which is the point of crack initiation. The analysis region was a square with a size of 300 nm by 300 nm around point B, Fig. 11a. The magnitude of maximum normal stress on different crystallographic planes was then plotted with respect to time for the atomic positions within the box, Fig. 11b. Like the 1120 cutting direction, tensile normal stress on the C-plane showed a higher value compared to other crystal planes. Figure 11c shows the tensile normal stress on the C- plane at point B. As shown in Fig. 11c, the tensile normal stress on the C-plane dramatically decreased from 19 to 0 GPa at crack initiation. This trend was different from the case of $|\overline{1}100|$ cutting direction since the energy from accumulated stresses is released through crack opening as shown in the images in Fig. 11c (the crack is very small at initiation but the reduction in stresses through the color map is clearly visible). Figure 11d shows the shear stress on the basal C-plane and rhombohedral R-planes at point B. It shows a

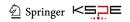


Fig. 9 For $\boxed{1120}$ cutting orientation, **a** selected area for stress analysis, **b** maximum normal stress on different planes among the points in the scanned area, **c** normal stress at point A, and **d** shear stress along the slip/twinning systems of the C-plane at point A

high amount of shear stress on the R- planes, compared to the C-plane. This can be explained by the fact that, for this cutting orientation, the slip and twinning systems, $C_{\rm sl1}$ and $C_{\rm tw2}$ are oriented at a steep angle with respect to the cutting direction and hence have a lower probability of activation.

From the analysis, it can be said that the material removal behavior observed in MD simulations could be better understood using the normal and shear stresses acting on each crystal plane. For the case of $\boxed{1120}$ cutting direction, most of the cutting energy was directed on the C-plane and only a small amount of the stress was accumulated compared to $\boxed{1100}$ cutting direction. In the case of $\boxed{1100}$ cutting direction, basal mechanisms were not as prominent due to the unfavorable geometric alignment of the systems and as a result, rhombohedral twinning was dominant.

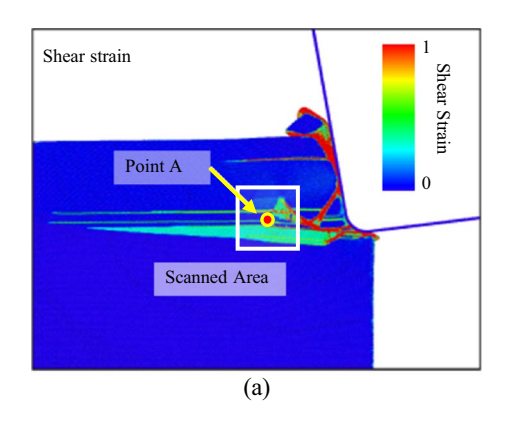
4.2 Comparison of Plastic deformation and Cleavage Fracture Parameters Between Experiment and MD Based Results

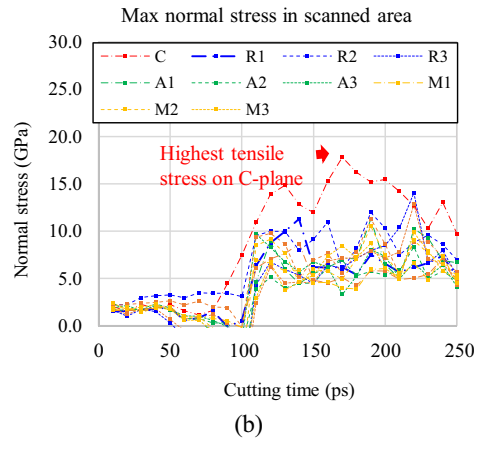
In Sect. 4.1, the normal and shear stress analysis provide a good insight into the distribution of stresses on different crystal planes. However, as the critical activation values for different systems can vary largely, it is important to consider these values to fully understand material deformation during machining of ceramics. This was addressed using the plastic deformation and cleavage fracture parameters calculated based on force from experimental measurements and stress from MD simulations following the method introduced in Sect. 2.3.

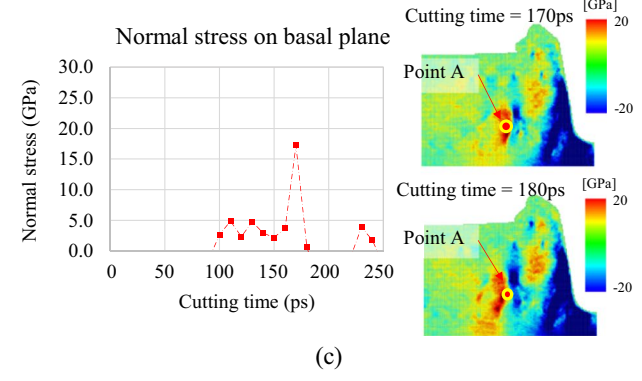
For the calculations based on experiments, the force data was analyzed up to the critical depth of cut. In the experiments, cracks were easily generated in the $\left[\overline{1}100\right]$ cutting direction compared to the $\left[\overline{1}120\right]$ cutting direction, which matched the MD simulation results.

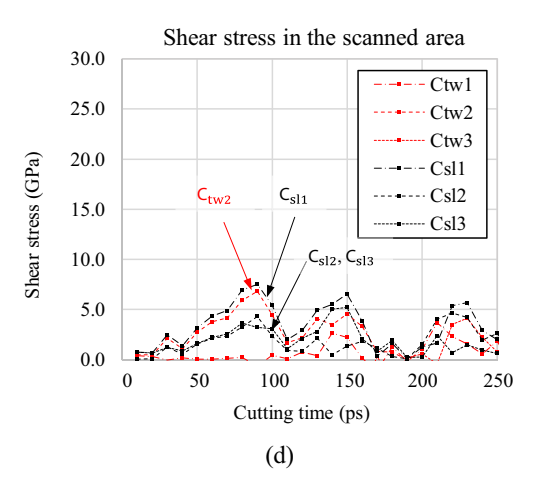
Extending the results from Sect. 4.1, plastic deformation and cleavage fracture parameter calculations were performed at all points within the scanned area and an average value is presented. Since the plastic deformation and cleavage fracture parameters on the 1st prismatic (A-) and 2nd prismatic (M-) systems were relatively small for both MD simulations and experiments, they were ignored in this study.

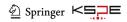
Figures 12 and 13 show the plastic deformation and cleavage fracture parameters calculated based on MD











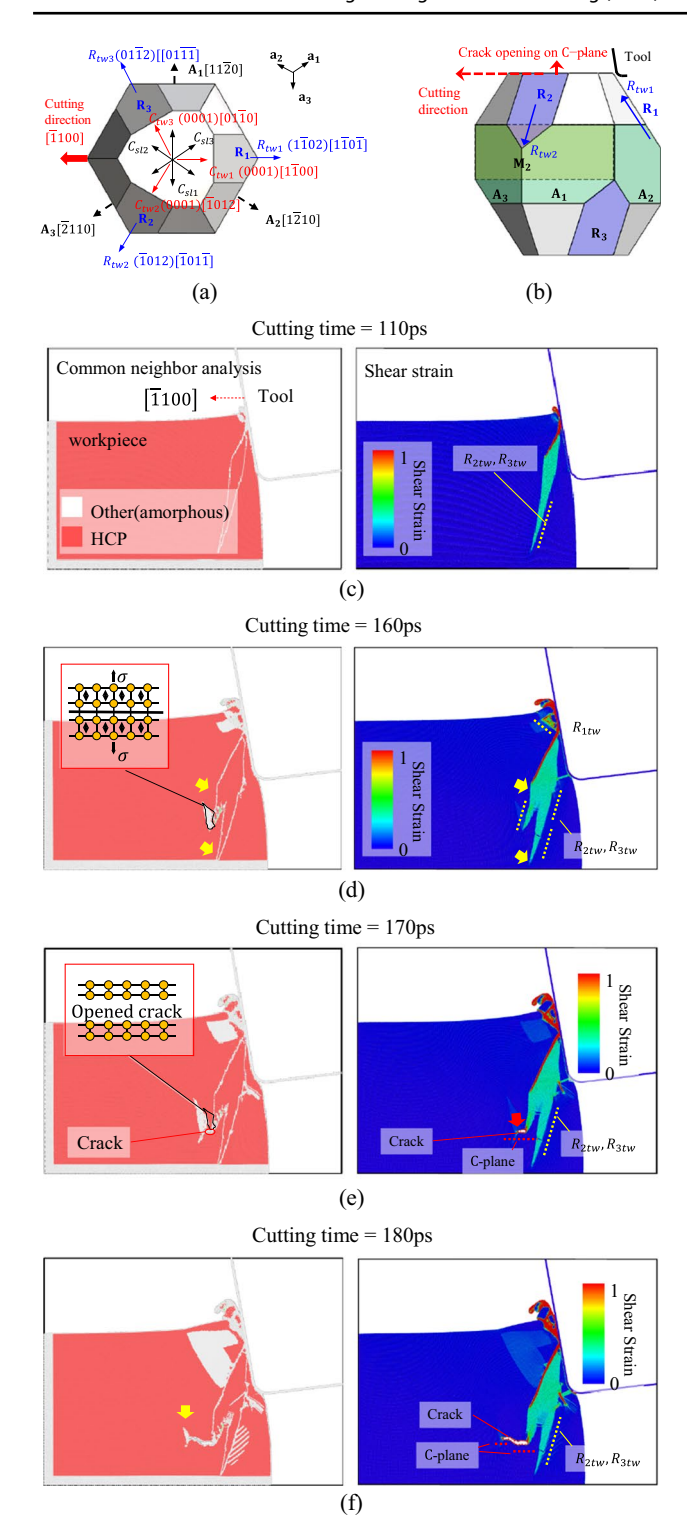


Fig. 10 The schematic view of cutting orientation in **a** top view and **b** side view. Shear strain and common neighbor analysis in terms of cutting time at **c** 110 ps, **d** 160 ps, **e** 170 ps, and **f** 180 ps. Crack initiation occurred at a cutting time of 170 ps

simulation and experimental results along the $[\overline{11}20]$ and $[\overline{11}00]$ directions, respectively. Compared to stress plots in Figs. 9 and 11, these parameters do not show any clear peaks, but smooth trends as shown in Figs. 12a–d and 13a–d.

Figure 12a, b show the plastic deformation and cleavage fracture parameters from MD simulations along the $\boxed{11}20$ direction. At the initial stages of cutting, multiple plastic deformation parameters on the C-plane were prominent, Fig. 12a. As the cutting progressed, cleavage fracture parameter on the rhombohedral R_2 -plane and C-plane became dominant, Fig. 12b. In the MD simulations, a crack initiation was not observed in this direction due to reasons explained in Sect. 4.1. Because of dominance of basal slip and twinning, Fig. 12a, the plastically deformed material does not extend deep into the workpiece. As a result, the deformed material is continuously removed by chip formation with minimal stress accumulation in front of the tool which delays crack initiation.

Figure 12c, d show calculated plastic deformation and cleavage fracture parameters from experiments along the $\boxed{1120}$ direction. Figure 12c shows that slip and twinning on the C-plane, dominant C_{sl1} , C_{sl2} , C_{sl3} , and C_{tw3} . These results were similar to the calculations based on MD simulations in that multiple plastic deformation systems on the C-plane were dominant. In the case of experiments, higher probability of twinning on the rhombohedral R_2 -plane was observed as the cutting progressed which was not seen in the case of MD simulations.

Figure 12b, d show differences in the calculation of cleavage fracture parameter between MD simulations and experiments, respectively. Both MD simulations and experiment-based calculations, show an increase in the R_3 -cleavage parameter, consistent value of R_1 -cleavage and reduction in the R_2 -cleavage parameter as the cutting progresses. Basal cleavage showed a slightly different trend in the MD simulations compared to experimental results where a decreasing trend was observed. However, in both cases, basal cleavage had the second or third highest activation probability.

Figure 13a, b show the plastic deformation and cleavage fracture parameters from MD simulations along the $\begin{bmatrix} \overline{1}100 \end{bmatrix}$ direction. The plastic deformation parameter of rhombohedral R_2 - and R_3 -planes were high at the beginning of cutting. As the cutting progresses, these parameters became zero at 20 ps. The value of most plastic deformation parameters on C-plane were low, Fig. 13a. In terms of the cleavage fracture parameter, Fig. 13b, rhombohedral cleavages (R_2 , R_3) were

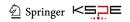


Fig. 11 For $[\overline{1}100]$ cutting orientation, **a** selected area for stress analysis, **b** maximum normal stress on different planes among the points in the scanned area, **c** normal stress at point B, and **d** shear stress along the slip/twinning systems on C-plane at point B

initially dominant, but the basal cleavage mechanism started to increase around 70 ps and became dominant at 110 ps.

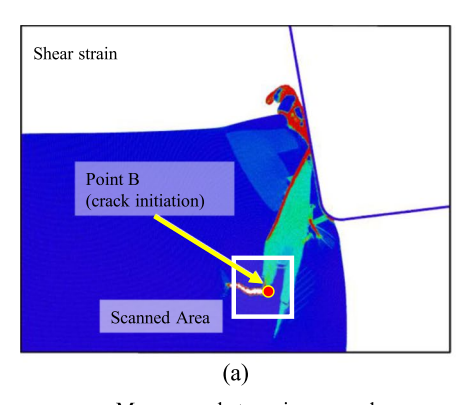
The MD simulations showed that a crack opened parallel to the C-plane normal at a cutting time of 170 ps. The primary reason for crack initiation was stress accumulation at the beginning of cutting by activation of rhombohedral twinning on R₂- and R₃-planes. As the cutting progressed and basal cleavage parameter increased, the already accumulated stress facilitated crack initiation.

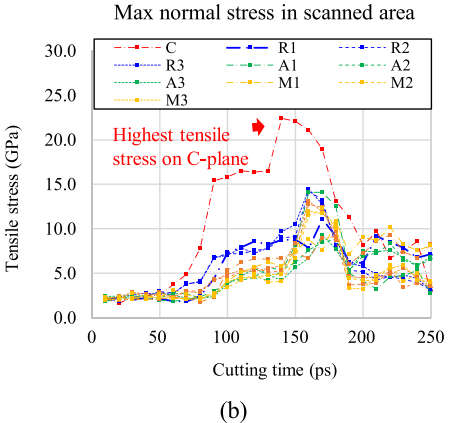
Figure 13c, d show the plastic deformation and cleavage fracture parameters from experiments along the $\left[\overline{1}100\right]$ direction. In terms of the plastic deformation parameters, C_{tw1} , C_{sl2} , and C_{sl3} were dominant, Fig. 13c. This result varied from MD simulations where dominance of twinning on the rhombohedral plane was predicted Fig. 13a. Looking at the cleavage fracture parameters in Fig. 13d, although the absolute values varied between the MD simulations and experiments, the overall trends were similar. R_2 - and R_3 -cleavage parameters decreased as the cutting progressed whereas R_1 -cleavage showed an increasing trend. However, like the case of $\left[\overline{11}20\right]$ cutting orientation, basal cleavage showed some discrepancies between MD simulation and experiments.

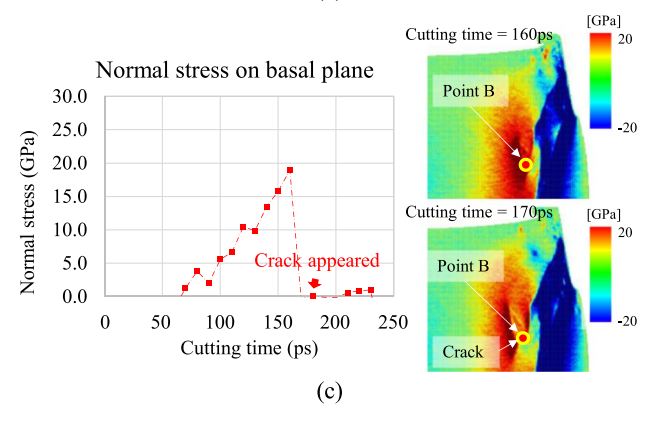
One of the reasons for the differences may come from the fact that plastic deformation/cleavage fracture parameters from MD simulations are uniaxial calculations considering only the maximum principal stress. Also, differences in the strain rates between experiments and simulations could cause differences in the stress state which could lead to different deformation mechanism activations or trends.

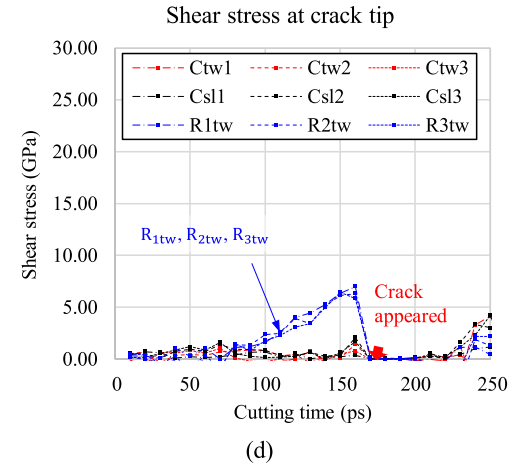
Figure 14 shows the crack shape in MD simulations, and SEM image of surface cracks in the $[\overline{1}100]$ cutting direction. As the MD simulation uses a thin width with periodic boundary conditions to simulate orthogonal cutting, effects of the tool nose radius and differences in the stresses along the lateral direction make it difficult to fully understand the 3-dimensional crack morphology.

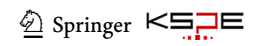
However, useful insight in terms of crack initiation and propagation along specific cleavage planes was obtained. The crack observed in the MD simulation created a new surface parallel to the C-plane. As the cutting progresses, it is expected that the material above the new surface is layered, having a morphology similar to that observed in experiments (Fig. 14b).











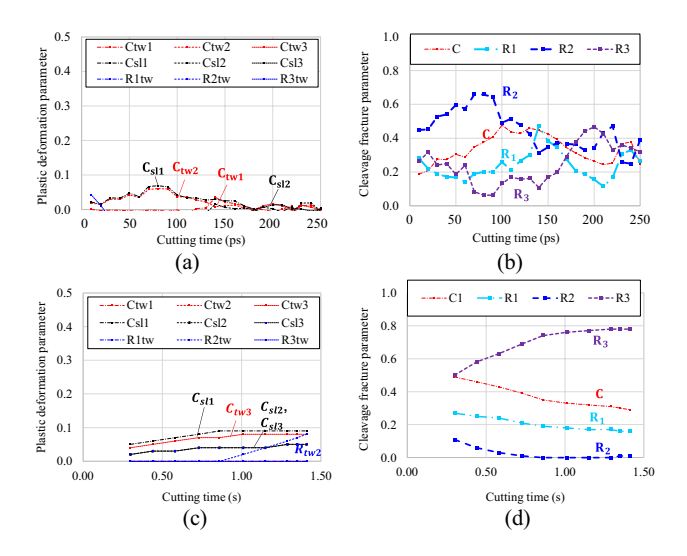


Fig. 12 Calculation along $[\overline{11}20]$ direction of, MD simulation- based a plastic deformation parameters and **b** cleavage fracture parameters. And experimental based \mathbf{c} plastic deformation parameters and \mathbf{d} cleavage fracture parameters

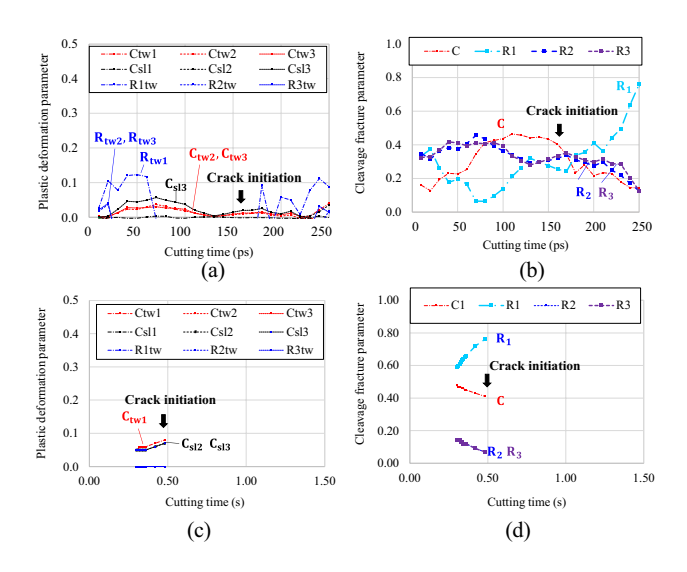


Fig. 13 Calculations along $\lceil \overline{1}100 \rceil$ direction of, MD simulation-based a plastic deformation parameters and **b** cleavage fracture parameters. And experimental based **c** plastic deformation parameters and **d** cleavage fracture parameters

5 Conclusion

In this study, material deformation during ultra-precision machining on C-plane of sapphire was investigated by calculating the normal and shear stresses on different crystallographic planes and the likelihood of activation of different plastic deformation and fracture systems through MD simulations which were then compared to experimental results.

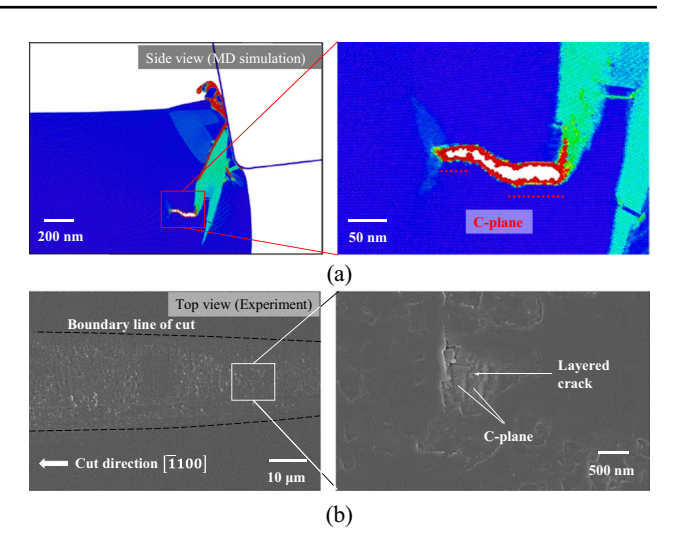
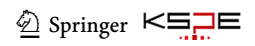


Fig. 14 Crack generation from $\bf a$ the MD simulation and $\bf b$ the experiment along $\begin{bmatrix} \overline{1}100 \end{bmatrix}$ cutting direction

Along the two cutting directions investigated, crack initiation was observed in the MD simulations along the 1100 cutting direction but not the 1120 cutting direction. This is likely due to the dominance of basal slip and twinning systems in the $|\overline{11}20|$ direction which causes shallow plastic deformation that is consequently removed by chip formation which does not lead to much stress accumulation in front of the tool. The iterative accumulation and release of shear strain observed also support this idea of stress relief in front of the tool. In the case of the $\boxed{1100}$ cutting direction, due to the dominance of the rhombohedral twinning mechanism which extends deeper into the substrate leads to stress accumulation and subsequent crack initiation. Further, high value of tensile normal stress on the basal plane and shear stress on the rhombohedral plane promotes crack initiation. MD simulations predicted cleavage on the basal plane which was also observed in the SEM observations from experiments.

Going forward, it would be useful to consider second and third principal stresses in the calculation of the plastic deformation and fracture cleavage parameters. Further, this novel analysis methodology can be extended to study material deformation along different cutting orientations in sapphire as well as different process parameters.

Acknowledgements Authors gratefully acknowledge the kind support from FANUC Corporation, Japan, for the donation of ROBONANO α -0*i*B, ultra-precision machine tool and A.L.M.T. Corporation, Japan, for providing discounted PCD tools to MIN LAB at UW-Madison. This material is based on work supported by the National Science Foundation under Grant No. CMMI-1844821, No. CMMI-2008563 and No. CMMI-2009150. The authors gratefully acknowledge use of facilities and instrumentation at the UW-Madison Wisconsin Centers for Nanoscale Technology (wcnt.wisc.edu) partially supported by the

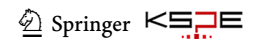


NSF through the University of Wisconsin Materials Research Science and Engineering Center (DMR-1720415).

References

- Akselrod, M. S., & Bruni, F. J. (2012). Modern trends in crystal growth and new applications of sapphire. *Journal of Crystal Growth*, 360, 134–145. https://doi.org/10.1016/j.jcrysgro.2011. 12.038
- Dobrovinskaya, E. R., Lytvynov, L. A., & Pishchik, V. (2009). Sapphire: material, manufacturing, applications.
- 3. Xu, Y., Yamazaki, M., & Villars, P. (2011). Inorganic materials database for exploring the nature of material. *Japanese Journal of Applied Physics*, 50(11S), 11RH02.
- Johnson-Walls, D., Evans, A. G., Marshall, D. B., & James, M. R. (1986). Residual stresses in machined ceramic surfaces. *Journal of the American Ceramic Society*, 69(1), 44–47.
- Mizumoto, Y., Maas, P., Kakinuma, Y., & Min, S. (2017). Investigation of the cutting mechanisms and the anisotropic ductility of monocrystalline sapphire. CIRP Annals, 66(1), 89–92. https://doi.org/10.1016/j.cirp.2017.04.018
- Kwon, S. B., Nagaraj, A., Yoon, H.-S., & Min, S. (2020). Study
 of material removal behavior on R-plane of sapphire during
 ultra-precision machining based on modified slip-fracture
 model. Nanotechnology and Precision Engineering, 3(3),
 141-155
- Hayama, Y., Fujii, S., Tanabe, T., & Kakinuma, Y. (2022). Theoretical approach on the critical depth of cut of single crystal MgF2 and application to a microcavity. *Precision Engineering*, 73, 234–243
- 8. Yoon, H.-S., Kwon, S. B., Nagaraj, A., & Min, S. (2019). Investigation of the ductile cutting behavior of monocrystal-line Yttria-stabilized zirconia during ultra-precision orthogonal cutting. *International Journal of Precision Engineering and Manufacturing*, 20(9), 1475–1484.
- Mizumoto, Y., & Kakinuma, Y. (2018). Revisit of the anisotropic deformation behavior of single-crystal CaF2 in orthogonal cutting. *Precision Engineering*, 53, 9–16.
- Dai, H., Li, S., & Chen, G. (2019). Molecular dynamics simulation of subsurface damage mechanism during nanoscratching of single crystal silicon. *Proceedings of the Institution of Mechanical Engineers*, Part J: Journal of Engineering Tribology, 233(1), 61–73.
- 11. Dai, H., Li, S., & Chen, G. (2018). Comparison of subsurface damages on mono-crystalline silicon between traditional nanoscale machining and laser-assisted nanoscale machining via molecular dynamics simulation. Nuclear Instruments and Methods in Physics Research Section B: Beam Interactions with Materials and Atoms, 414, 61–67.
- Li, J., Fang, Q., Liu, Y., & Zhang, L. (2014). A molecular dynamics investigation into the mechanisms of subsurface damage and material removal of monocrystalline copper subjected to nanoscale high speed grinding. *Applied Surface Science*, 303, 331–343.
- 13. Liu, Y., Li, B., & Kong, L. (2018). Molecular dynamics simulation of silicon carbide nanoscale material removal behavior. *Ceramics International*, 44(10), 11910–11913.
- Liu, Y., Li, B., Wu, C., Kong, L., & Zheng, Y. (2018). Smoothed particle hydrodynamics simulation and experimental analysis of SiC ceramic grinding mechanism. *Ceramics International*, 44(11), 12194–12203.
- Dai, H., Chen, G., Fang, Q., & Yin, J. (2016). The effect of tool geometry on subsurface damage and material removal in

- nanometric cutting single-crystal silicon by a molecular dynamics simulation. *Applied Physics A*, 122(9), 1–16.
- Fang, Q., Wang, Q., Li, J., Zeng, X., & Liu, Y. (2017). Mechanisms of subsurface damage and material removal during high speed grinding processes in Ni/Cu multilayers using a molecular dynamics study. RSC advances, 7(67), 42047–42055.
- Chang, J., Bodur, C. T., & Argon, A. S. (2003). Pyramidal edge dislocation cores in sapphire. *Philosophical magazine letters*, 83(11), 659–666.
- Wunderlich, W., & Awaji, H. (2000). Molecular dynamicssimulations of the fracture toughness of sapphire. *Progress of Theoretical Physics Supplement*, 138, 156–158.
- 19. Kuksin, A. Y., & Yanilkin, A. V. (2012). Formation of twins in sapphire under shock wave loading: Atomistic simulations. *Journal of Applied Physics*, 111(3), 033513.
- Nishimura, K., Kalia, R. K., Nakano, A., & Vashishta, P. (2008).
 Nanoindentation hardness anisotropy of alumina crystal: A molecular dynamics study. Applied Physics Letters, 92(16), 161904.
- Lin, J., Jiang, F., Xu, X., Lu, J., Tian, Z., Wen, Q., & Lu, X. (2021). Molecular dynamics simulation of nanoindentation on c-plane sapphire. *Mechanics of Materials*, 154, 103716.
- Kim, W. K., Xi, D., & Kim, B. H. (2019). Nanoscale indentation and scratching tests of single crystal sapphire using molecular dynamics simulation. *Computational Materials Science*, 170, 109195
- Kim, W. K., & Kim, B. H. (2017). A molecular dynamics study on atomistic mechanisms of nano-scale cutting process of sapphire. *Journal of Mechanical Science and Technology*, 31(9), 4353–4362
- 24. Wang, N., Jiang, F., Xu, X., & Lu, X. (2017). Effects of crystal orientation on the crack propagation of sapphire by sequential indentation testing. *Crystals*, 8(1), 3.
- Thompson, A. P., Aktulga, H. M., Berger, R., Bolintineanu, D. S., Brown, W. M., Crozier, P. S., Veld, P. J., & in't, Kohlmeyer A, Moore SG, Nguyen TD,. (2022). LAMMPS-a flexible simulation tool for particle-based materials modeling at the atomic, meso, and continuum scales. *Computer Physics Communications*, 271, 108171.
- Choudhary, K., Liang, T., Chernatynskiy, A., Phillpot, S. R., & Sinnott, S. B. (2015). Charge optimized many-body (COMB) potential for Al₂O₃ materials, interfaces, and nanostructures. *Journal of Physics: Condensed Matter*, 27(30), 305004.
- Sekkal, W., & Zaoui, A. (2009). A modified embedded atom method for the corundum and the bixbyite forms of alumina: Bulk and surface studies. *Physica B: Condensed Matter*, 404(2), 335–339
- Gale, J. D., Catlow, C. R. A., & Mackrodt, W. C. (1992). Periodic ab initio determination of interatomic potentials for alumina. Modelling and simulation in materials science and engineering, 1(1), 73.
- Vashishta, P., Kalia, R. K., Nakano, A., & Rino, J. P. (2008). Interaction potentials for alumina and molecular dynamics simulations of amorphous and liquid alumina. *Journal of Applied Physics*, 103(8), 083504.
- Yu, J., Sinnott, S. B., & Phillpot, S. R. (2007). Charge optimized many-body potential for the Si/SiO2 system. *Physical Review B*, 75(8), 085311.
- 31. Clayton, J. D. (2009). A continuum description of nonlinear elasticity, slip and twinning, with application to sapphire. *Proceedings of the Royal Society A: Mathematical, Physical and Engineering Sciences*, 465(2101), 307–334.
- Iwasa, M., & Bradt, R. C. (1984). Fracture toughness of singlecrystal alumina. Advances in ceramics, 10, 767.



33. Stukowski, A. (2009). Visualization and analysis of atomistic simulation data with OVITO-the open visualization tool. *Modelling and simulation in materials science and engineering*, 18(1), 015012.

Publisher's Note Springer Nature remains neutral with regard to jurisdictional claims in published maps and institutional affiliations.

Springer Nature or its licensor (e.g. a society or other partner) holds exclusive rights to this article under a publishing agreement with the author(s) or other rightsholder(s); author self-archiving of the accepted manuscript version of this article is solely governed by the terms of such publishing agreement and applicable law.



Suk Bum Kwon is a Postdoctoral researcher in the Department of Mechanical Engineering, University of Wisconsin-Madison, Wisconsin, United States. His research interests include modeling anisotropic material removal behavior in ultra-precision machining (UPM) of single-crystal ceramics, understanding crack generation mechanisms, and coating effect during machining.



Aditya Nagaraj is a Ph.D. candidate in the Department of Mechanical Engineering, University of Wisconsin-Madison, Wisconsin, United States. His research interests include ultraprecision machining of single crystalline ceramics, residual stresses, and subsurface damage formation during machining.



Dalei Xi is a Ph.D. candidate in the Department of Mechanical and Materials Engineering at the University of Cincinnati. His research interests include atomistic simulations of ultra-precision machining, deformation and fracture mechanism of single crystalline ceramics.



Yiyang Du is a Ph.D. candidate in the Department of Mechanical and Materials Engineering at the University of Cincinnati. His research interests include atomistic simulations of ultra-precision machining, deformation and fracture mechanism of single crystalline ceramics.



Dae Nyoung Kim is a Ph.D. candidate in the Department of Mechanical Engineering, University of Wisconsin-Madison, Wisconsin, United States. His research interests include ultraprecision machining of single crystalline ceramics, crack generation mechanism, and anisotropic material behavior during machining.



Woo Kyun Kim is an Associate Professor in the Department of Mechanical and Materials Engineering at the University of Cincinnati. His research interests include atomistic simulations and multiscale modeling about crystal defects and deformation, fracture, friction, and 2-D materials.



Sangkee Min is an associate professor at Department of Mechanical Engineering, University of Wisconsin-Madison and a director of Manufacturing Innovation Network Laboratory (MIN Lab: https://min.me.wisc.edu/). He is currently working on three major research topics: UPM (Ultra-Precision Machining), SSM (Smart Sustainable Manufacturing), and MFD (Manufacturing for Design).

